

Asymmetric Silver “Nanocarrot” Structures: Solution Synthesis and Their Asymmetric Plasmonic Resonances

Hongyan Liang,[†] David Rossouw,[‡] Haiguang Zhao,[†] Scott K. Cushing,[§] Honglong Shi,^{||} Andreas Korinek,[‡] Hongxing Xu,[‡] Federico Rosei,[†] Wenzhong Wang,^{||} Nianqiang Wu,[§] Gianluigi A. Botton,[‡] and Dongling Ma^{*,†}

[†]INRS-EMT, Université du Québec, 1650 Boul. Lionel-Boulet, Varennes, QC, Canada J3X 1S2

[‡]Department of Materials Science and Engineering, McMaster University, 1280 Main Street West, Hamilton, ON, Canada L8S 4L7

[§]Department of Mechanical & Aerospace Engineering, West Virginia University, Morgantown, West Virginia 26506, United States

^{||}School of Science, Minzu University of China, Beijing 100081, P. R. China

^{*}Institute of Physics, Chinese Academy of Sciences, Beijing 100190, P. R. China

Supporting Information

ABSTRACT: Here we report the wet-chemical synthesis of asymmetric one-dimensional (1D) silver “nanocarrot” structures that exhibit mixed twins and stacking fault domains along the $\langle 111 \rangle$ direction. Oriented attachment is the dominant mechanism for anisotropic growth. Multipolar plasmon resonances up to fourth order were measured by optical extinction spectroscopy and electron energy-loss spectroscopy (EELS) and are in agreement with theoretical calculations. Compared with those of symmetric 1D nanostructures of similar length, the dipole modes of the nanocarrots show a clear red shift, and the EELS maps show an asymmetric distribution of the resonant plasmonic fields and a compression of the resonance node spacing toward the tail. In addition, increasing the length of the nanocarrots causes an increase in the intensity and a steady red shift of the longitudinal surface plasmon resonance peaks. The silver nanocarrots also show very high sensitivity to the refractive index of their environment (890 ± 87 nm per refractive index unit).

One-dimensional (1D) metallic nanostructures have been widely studied because of their unique electronic and photonic properties.¹ An incident electric field can excite surface plasmons at the metal–dielectric interface. The surface plasmon resonance (SPR) energy is highly sensitive to the composition, size, morphology, incident excitation, and local environment of a nanoscale system. The position of the SPR resonance in the electromagnetic (EM) spectrum, the sensitivity of the SPR energy to the local dielectric environment, and the ability of SPR to concentrate and enhance the local EM field intensity below the diffraction limit can result in many applications.² Thus, precise control of the size and morphology of metallic nanostructures is critical for tuning the SPR energy and intensity as well as improving the efficiency of light manipulation.

1D silver nanostructures support both transverse and longitudinal resonances, with the latter tunable from the visible to the near-IR (NIR) spectral range by variation of the aspect ratio (length/diameter).^{1,3} With increasing aspect ratio, higher-order multipolar SPR modes that behave like Fabry–Pérot (FP)

resonators can be excited.^{4,5} Moreover, “dark” modes in elongated 1D nanostructures⁵ are imperative for sub-diffraction-limit waveguiding without radiative loss. Fueled by these broad possibilities, various 1D silver nanostructures have been synthesized, including nanowires,¹ nanobars,^{3a,6} and nanorices.^{3a,6,7} Generally, 1D nanostructures are highly symmetric because the crystal symmetry of the face-centered cubic (fcc) structure inhibits asymmetric growth. Rare examples of asymmetric 1D nanostructures have been reported,⁸ but corresponding analysis of the plasmonic properties is lacking. Studying the relationship between the structure and optical properties of metal nanostructures requires characterization techniques that combine high spatial and energy resolution. Traditional far-field optical excitation techniques exhibit excellent spectral resolution, but their spatial resolution is constrained by the light diffraction limit.^{4a} Electron energy-loss spectroscopy (EELS) is an alternative technique that offers high spatial resolution (<1 nm) and access to information in the UV–vis–NIR range.^{4,5,9} The electron beam can also probe both bright and dark modes and hence unravel the full modal spectrum of a plasmonic nanostructure.^{4a,9b} Here we report the synthesis, structure, and plasmonic properties of novel carrot-shaped asymmetric silver nanostructures (“nanocarrots”).

The nanocarrots were synthesized through a polyol approach. The main difference from the synthesis of silver nanorice structures was that CF_3COOAg instead of AgNO_3 was used as the precursor.^{6,7} This approach led to the formation of a uniform asymmetric 1D structure with a tapered tail and a broad head, as clearly revealed by transmission electron microscopy (TEM) (Figure 1a). Large-area and tilted scanning electron microscopy (SEM) images as well as thickness measurements on an individual nanocarrot showed that the nanocarrots have a conical shape [Figure S1 in the Supporting Information (SI)]. A detailed characterization of the crystal structure was performed with high-resolution TEM (HRTEM), powder X-ray diffraction (PXRD), and selected-area electron diffraction (SAED). The HRTEM images demonstrate that the growth took place along

Received: May 1, 2013

Published: June 11, 2013

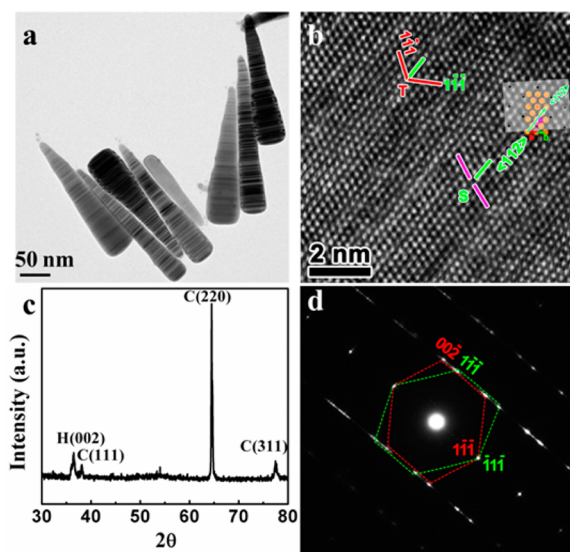


Figure 1. (a) TEM image and (c) PXRD pattern of silver nanocarrots. (b) HRTEM image and (d) corresponding SAED pattern taken from the center part of an individual nanocarrot. In (b), twins and stacking faults are labeled as T and S, respectively.

the $\langle 111 \rangle$ direction (Figures 1b and S2). In our TEM experiments, electron beam was nearly parallel to the $[110]$ zone axis. The common indexing of this pattern is shown in Figure 1d, where two sets of diffraction spots from the twins and matrix are indicated by the green and red polygons, respectively. Obviously, the coincident lattice planes are $(1\bar{1}1)$ and $(11\bar{1})$, which are marked as the green bar in the “T” area in Figure 1b [the two equivalent lattice planes of $\{111\}$ can be obtained by a reflection operation on a specific (111) plane]. The lattice direction of atoms on these coincident planes is the $\langle 112 \rangle$ direction, that is, on $\{111\}$ planes stacked along the $\langle 112 \rangle$ directions (marked as purple bars in the “S” area). However, this stacking is often not perfect and exhibits stacking faults: the purple bars highlight the misfit, which can be directly observed in the HRTEM image. A small amount of hexagonal close-packed (hcp) phase due to the A–B–A–B stacking occasionally visible in the HRTEM images was also present, as confirmed by the PXRD pattern (Figure 1c), which contained a weak peak at 36.4° assigned to the (002) family of the hcp phase in addition to three typical peaks indexed to the silver fcc phase. It is clear that in the nanocarrot structure the fcc phase dominates.

The crystal structure of the nanocarrots is similar to that of the nanorice reported previously,^{6,7} and the basic growth mechanism is also expected to be similar: seeds selected through oxygen etching feed the elongated growth via oriented attachment combined with lateral growth governed by Ostwald ripening.⁶ Herein, instead of AgNO_3 , the more stable $\text{CF}_3\text{COOAg}^{10}$ was employed as the precursor, leading to slower growth and an extension of the seed selection time period. In this situation, some seeds are prone to grow larger before they adhere to the 1D nanostructure (Figure S3). When their size is larger than a critical value, they become much more stable than smaller seeds. Once attached with smaller seeds and/or 1D nanostructures in solution, they stabilize the structure at their end by inhibiting further oriented attachment on them. As a result, longitudinal growth based on oriented attachment is terminated at the end capped by a relatively large seed, and lateral growth by deposition of diffused metal adatoms becomes favorable, which eventually leads to the growth of a broad head. Such larger-crystal-related

end-termination growth behavior has also been reported in the synthesis of nanobars,⁶ which have similar broad ends. The difference may be that the quantity of large seeds formed through the slow growth reported herein is not sufficient to terminate both ends, resulting in the formation of the asymmetric structure. This hypothesis provides some insights for the controlled formation of asymmetric or symmetric 1D nanostructures. The growth mechanism will be investigated in future work.

The study of SPR excitations in nanoscale structures is well-suited to analysis by EELS, where plasmonic oscillations are excited by the transient field of the electrons.¹¹ The optical extinction spectrum was measured with far-field optical excitation as well as calculated and further compared with nanoscale EELS characterization. Figure 2 displays the extinction

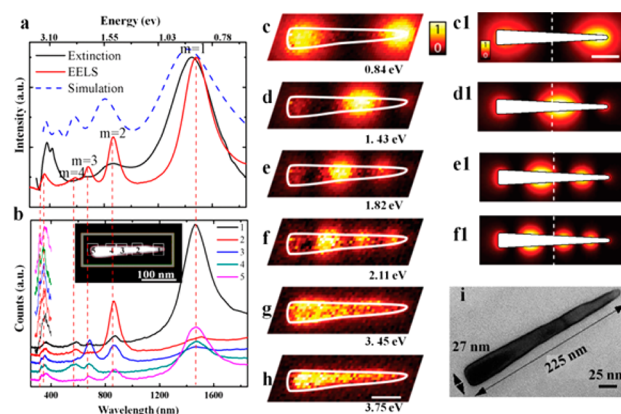


Figure 2. (a) Comparison of the EELS spectrum of the nanocarrot shown in (i) with the optical extinction spectrum of a nanocarrot ensemble and a simulated optical extinction spectrum obtained using the FDTD method. (b) EELS signals acquired at five different locations around the nanocarrot. The rectangular region defines the limits of the detected area for the total spectrum in (a). The spectra have been displaced vertically for clarity, and the transverse SPR peaks from locations 1–5 have been enlarged and vertically offset to improve the readability. The red dashed lines in (a) and (b) are guides to the eye joining identical resonance modes. (c–h) Experimental maps of multiple plasmon resonances excited in the nanocarrot extracted at energies belonging to the peaks in the EELS signal. (c1–f1) EELPs calculated from BEM probability maps, corresponding to the experimental maps in (c–f). The scale bars in (h) and (c1) are 50 nm. (i) TEM image of the nanocarrot chosen for EELS mapping.

spectrum for the bulk silver nanocarrot solution, the corresponding finite-difference time-domain (FDTD) simulation results, and the summed EELS spectrum along with energy-filtered maps extracted from an individual silver nanocarrot. The nanocarrots were identical to those shown in Figure 1a. We assign the peaks at 1449, 861, and 661 nm in the ensemble extinction spectrum to multipolar longitudinal plasmonic resonances of increasing order (m).¹² The EELS signal extracted from the individual silver nanocarrot shown in Figure 2i exhibits peaks at 0.84, 1.43, 1.82, 2.11, 3.45, 3.75 eV (1476, 867, 681, 587, 359, and 331 nm, respectively). The first four peaks correspond to the longitudinal SPR modes with $m = 1$ –4. The excitation at 3.45 eV, which shows a slight transverse character, is assigned to an SPR, while the excitation at 3.75 eV is assigned to the volume plasmon for silver.^{4a} With increasing m , the peak amplitude decreases. The EELS spectrum essentially shows similar features to the optical extinction spectrum. The broadening of the spectral features in the experimental optical extinction spectrum may be attributed

to the size/shape polydispersity.^{3b,4b} The FDTD method was used to calculate the optical extinction spectrum for a nanocarrot with the same dimensions, and the main features were reproduced. However, the calculated longitudinal SPR modes were blue-shifted in comparison with the experimental results because of deviations in the simulated geometry and refractive index (RI) from the experimental ones.^{4a,9b} The fourth-order ($m = 4$) mode resolved in the EELS spectrum could not be discerned in either the bulk optical measurement or the simulation, perhaps because of the spectral broadening and the weakness of the highest mode.

The measured EELS signals varied significantly with the electron probe position. The EELS signals collected from different locations of the nanocarrot are marked and displayed in Figure 2b. When the focused electron beam was positioned near the head or the tail, the $m = 1$ longitudinal mode was efficiently excited, whereas when the electron beam was placed at the middle, the $m = 2-4$ modes were excited. Under closer inspection, some subtle differences in the plasmonic responses at the head and tail were apparent. With excitation at the tail, the resonance intensity for the $m = 1$ mode was amplified and that of the $m = 3$ mode decreased. Upon excitation at the head, the $m = 1$ mode had a lower intensity and the $m = 4$ mode disappeared. We attribute these differences between the excitations at the two terminals to the asymmetric morphology, the different diameters, and the curvature along the long axis.

A series of energy-filtered maps (Figure 2c–h) were extracted by selectively filtering the scattering intensity belonging to each peak in the summed EELS spectrum. These revealed further information about the spatial character of each resonance. In our experiment, the impinging electron beam was perpendicular to the substrate, and the spatial origin of each SPR was observed. We interpret the observed standing-wave patterns in the EELS maps as being due to the interference of counterpropagating surface plasmon polaritons (SPPs). The maps resemble the standing-wave patterns observed for nanorod structures,^{5,13} which have been accurately modeled as FP resonators.⁵ Four longitudinal modes corresponding to FP-type resonances can be clearly discerned in Figure 2c–f, and the transverse SPR modes and bulk plasmon mode are imaged in Figure 2g,h, respectively. The normalized intensity in the maps reflects the electron energy loss probability (EELP). Variations in the signal strength and distribution from mode to mode are apparent. For the dipolar mode, the EELS signal extends appreciably outside the nanostructure and the intensity is higher near the tail, where excitation of the dipolar mode is most efficient (Figure 2b,c). Higher-order resonances are enumerated by the number of nodes crossed along the long axis of the nanocarrot. There is a clear asymmetry in the distribution of the nodes along this axis. The central nodes in the $m = 2$ and $m = 3$ modes are all displaced toward the sharp tail (Figure 2d and 2e). To confirm and aid the interpretation of the experimental results, we performed numerical simulations. Figure 2c1–f1 displays calculated EELPs for a nanocarrot at resonance.¹⁴ The calculated plots are in excellent agreement with the experimental energy-filtered EELS maps with respect to both the energy and spatial distribution, and the asymmetry at resonance is accurately reproduced. In summary, the silver nanocarrot structure supports both transverse and multipolar longitudinal modes whose nodes are displaced toward the tail of the nanocarrot.

Figure 3 compares the plasmonic responses of an asymmetric silver nanocarrot and a symmetric silver nanorod as measured by EELS. The asymmetry in the response of the nanocarrot over the

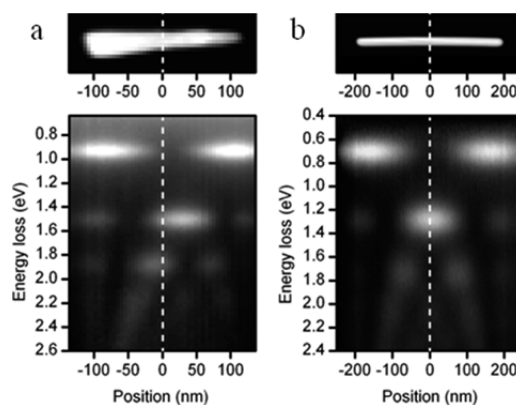


Figure 3. Comparison of the plasmonic responses of (a) an asymmetric nanocarrot and (b) a symmetric nanorod.

entire energy loss range is noticeable in the general displacement of the excited near-field maxima toward the tail of the nanocarrot (Figure 3a). The line profiles of the longitudinal resonances shown in Figure S4 provide a direct spatial correlation between the local enhanced EM field and the underlying structure. The distances between adjacent peaks for a given SPR mode decrease in going toward the tail of the nanocarrot. The symmetric plasmonic response of the symmetric nanorod (Figure 3b), which was reproduced by simulation results (Figure S5), supports the argument that the asymmetric plasmonic response of the nanocarrot is due to the asymmetry in its underlying structure. The asymmetric high-order pattern might be caused by the variations in the speed of the SPPs, which depends on the diameter of the cylinder: for a thinner cylinder, the SPPs are more localized and move more slowly.¹⁵ This seems to provide a qualitative explanation of the bias of the nodes toward the tail (i.e., the narrower part), where the SPPs would be anticipated to propagate more slowly than in the broader part. It is worth pointing out that a sharp tip can give a huge field enhancement due to this kind of propagation and localization of SPPs. This is also called “self-focusing”, which is important for applications such as surface-enhanced spectroscopy.^{2a,b}

The longitudinal resonances of the nanocarrot can be tuned by changing the length through variation of the reaction parameters. The solid lines in Figure S6a show the UV–vis–NIR extinction spectra of five sample batches of nanocarrots with different average lengths in poly(ethylene glycol) 600 (PEG 600) solution. The synthesis details are shown in Table S1 in the SI. Despite the differences in the average length, the main spectral features of the different batches are similar. The optical modes were also investigated by FDTD simulation (dashed lines in Figure S6a). The length of the nanocarrots was taken from the TEM imaging statistics. All of the experimental features were reproduced in simulation results, although slight peak shifts were observed in some samples. The differences between the simulated and experimental data are due to deviations in the morphology and dielectric environment.

It is apparent that with increasing length the first three longitudinal modes are red-shifted and the relative intensity of the $m = 1$ mode with respect to the transverse resonance is also amplified. The SPR peak positions were plotted against the average length of the nanocarrots (Figure S6a) to elucidate the trends in Figure S6a, and a linear relationship. The longitudinal resonance peaks are red-shifted linearly with increasing nanocarrot length, and the shift is more obvious for lower-order resonances. This trend can be contrasted with that for the two

transverse resonances near 400 nm, whose peak positions do not vary significantly with the length. These observations are in good agreement with previous measurements on symmetric 1D nanostructures.^{3b,12,16} Nonetheless, some differences are also noticed. For example, in the vis–NIR region, four prominent longitudinal SPR modes of the nanocarrot can be resolved in the EELS spectrum, while only three can be discerned for the nanorice of comparable length. The relative intensity of the $m = 1$ resonance with respect to that of the transverse mode is significantly amplified, which may originate from the broken symmetry in the nanocarrot and the high curvature in the sharp tail. The peak of the dipolar mode of the nanocarrots with an average length of 250 nm is situated at 1717 nm, which is nearly 500 nm further into the NIR range than that of the nanorice (1241 nm) with even longer length (304 nm). A resonance with such a long wavelength is rare in silver nanostructures synthesized by wet-chemical methods.

The sensitivity of the nanocarrot SPR to the RI of the surrounding medium was investigated by examining the shift of the SPR peak in different dielectric media (ethanol/PEG 600 mixtures with various volume ratios). The dipolar plasmons exhibited a sensitivity of 890 ± 87 nm RIU⁻¹ (RIU = RI unit) (Figure S7), which is higher than that of most reported plasmonic structures and is comparable to that of the highly sensitive silver nanorice structures we reported previously (820 nm RIU⁻¹).⁶ The sharp tip and large aspect ratio are important reasons for the observed high sensitivity of the nanocarrot. Such high sensitivity makes the nanocarrots highly promising for sensor applications to monitor local environmental changes during chemical and biological processes.

In summary, asymmetric 1D silver nanocarrots were synthesized in high yield for the first time. Structural characterization showed that the fcc-dominated crystalline silver nanocarrot structure features mixed twins and stacking faults along the $\langle 111 \rangle$ longitudinal direction. The SPR characteristics were revealed by far-field UV–vis–NIR optical extinction spectroscopy on particle ensembles and by nanoscale EELS on individual nanocarrots. The results obtained using both techniques were further supported by theoretical calculations. The multipolar plasmon resonances observed by EELS showed an interesting asymmetric distribution over the length of the nanocarrot, in contrast to the symmetric distribution normally observed in a nanorod. The longitudinal SPR peaks were red-shifted and their relative intensity with respect to that of the transverse resonance was amplified in optical spectra with increasing nanocarrot length. Silver nanocarrots also showed high RI sensitivity (890 ± 87 nm RIU⁻¹), making them very attractive for sensor applications. In addition, these nanocarrots are also promising for, but not limited to, biological sample studies because of their tunable SPRs in the NIR spectral range and optical waveguiding below the diffraction limit.

■ ASSOCIATED CONTENT

Supporting Information

Experimental methods and additional data. This material is available free of charge via the Internet at <http://pubs.acs.org>.

■ AUTHOR INFORMATION

Corresponding Author

ma@emt.inrs.ca

Notes

The authors declare no competing financial interest.

■ ACKNOWLEDGMENTS

Financial support from NSERC and AEE is greatly appreciated. H.L. thanks MELS for the Merit Scholarship for Foreign Students. The EELS work was carried out at the Canadian Centre for Electron Microscopy, a national facility supported by NSERC and McMaster University. D.R. and G.A.B. thank NSERC for a Discovery Grant and Discovery Accelerator Supplement. D.R. thanks the Ontario Graduate Scholarship Program for partial funding. W.W. thanks the NNSFC (11074312) and the 985 Project (98507-010009, 98507-012009) for funding. N.W. thanks NSF (CBET-1233795) for support.

■ REFERENCES

- (1) Chen, J.; Wiley, B. J.; Xia, Y. *Langmuir* **2007**, *23*, 4120.
- (2) (a) Liang, H.; Li, Z.; Wang, W.; Wu, Y.; Xu, H. *Adv. Mater.* **2009**, *21*, 4614. (b) Lim, D.-K.; Jeon, K.-S.; Kim, H. M.; Nam, J.-M.; Suh, Y. D. *Nat. Mater.* **2010**, *9*, 60. (c) Skrabalak, S. E.; Chen, J.; Sun, Y.; Lu, X.; Au, L.; Copley, C. M.; Xia, Y. *Acc. Chem. Res.* **2008**, *41*, 1587.
- (3) (a) Wiley, B. J.; Chen, Y.; McLellan, J. M.; Xiong, Y.; Li, Z.-Y.; Ginger, D.; Xia, Y. *Nano Lett.* **2007**, *7*, 1032. (b) Wei, H.; Reyes-Coronado, A.; Nordlander, P.; Aizpurua, J.; Xu, H. *ACS Nano* **2010**, *4*, 2649.
- (4) (a) Nicoletti, O.; Wubs, M.; Mortensen, N. A.; Sigle, W.; van Aken, P. A.; Midgley, P. A. *Opt. Express* **2011**, *19*, 15371. (b) N'Gom, M.; Ringnald, J.; Mansfield, J. F.; Agarwal, A.; Kotov, N.; Zaluzec, N. J.; Norris, T. B. *Nano Lett.* **2008**, *8*, 3200.
- (5) Rossouw, D.; Couillard, M.; Vickery, J.; Kumacheva, E.; Botton, G. A. *Nano Lett.* **2011**, *11*, 1499.
- (6) Liang, H.; Zhao, H.; Rossouw, D.; Wang, W.; Xu, H.; Botton, G. A.; Ma, D. *Chem. Mater.* **2012**, *24*, 2339.
- (7) Liang, H.; Yang, H.; Wang, W.; Li, J.; Xu, H. *J. Am. Chem. Soc.* **2009**, *131*, 6068.
- (8) (a) Wang, J. H.; Yang, T. H.; Wu, W. W.; Chen, L. J.; Chen, C. H.; Chu, C. J. *Nanotechnology* **2006**, *17*, 719. (b) Shen, X. S.; Wang, G. Z.; Hong, X.; Xie, X.; Zhu, W.; Li, D. P. *J. Am. Chem. Soc.* **2009**, *131*, 10812. (c) Huang, X.; Li, S.; Wu, S.; Huang, Y.; Boey, F.; Gan, C. L.; Zhang, H. *Adv. Mater.* **2012**, *24*, 979.
- (9) (a) Alber, I.; Sigle, W.; Müller, S.; Neumann, R.; Picht, O.; Rauber, M.; van Aken, P. A.; Toimil-Molares, M. E. *ACS Nano* **2011**, *5*, 9845. (b) Rodríguez-González, B.; Attouchi, F.; Cardinal, M. F.; Myroshnychenko, V.; Stéphan, O.; Garcia de Abajo, F. J.; Liz-Marzán, L. M.; Kociak, M. *Langmuir* **2012**, *28*, 9063.
- (10) Zhang, Q. A.; Li, W. Y.; Wen, L. P.; Chen, J. Y.; Xia, Y. N. *Chem.—Eur. J.* **2010**, *16*, 10234.
- (11) Garcia de Abajo, F. J. *Rev. Mod. Phys.* **2010**, *82*, 209.
- (12) Bryant, G. W.; Garcia de Abajo, F. J.; Aizpurua, J. *Nano Lett.* **2008**, *8*, 631.
- (13) Guiton, B. S.; Iberi, V.; Li, S.; Leonard, D. N.; Parish, C. M.; Kotula, P. G.; Varela, M.; Schatz, G. C.; Pennycook, S. J.; Camden, J. P. *Nano Lett.* **2011**, *11*, 3482.
- (14) Hohenester, U.; Trügler, A. *Comput. Phys. Commun.* **2012**, *183*, 370.
- (15) Kolesov, R.; Grotz, B.; Balasubramanian, G.; Stohr, R. J.; Nicolet, A. A. L.; Hemmer, P. R.; Jelezko, F.; Wrachtrup, J. *Nat. Phys.* **2009**, *5*, 470.
- (16) Dorfmueller, J.; Vogelgesang, R.; Weitz, R. T.; Rockstuhl, C.; Etrich, C.; Pertsch, T.; Lederer, F.; Kern, K. *Nano Lett.* **2009**, *9*, 2372.